Characterization of transient and progressive pulmonary fibrosis by spatially correlated phase contrast microCT, classical histopathology and atomic force microscopy

Lorenzo D'Amico [a,b], Angelika Svetlove [c,d], Elena Longo [b], Ruth Meyer [e], Beatrice Senigagliesi [f], Giulia Saccomano [b,g], Philipp Nolte [h,i], Willi L. Wagner [j], Mark O. Wielpütz [j], Dominik H.W. Leitz [k,l,m], Julia Duerr [k,l,m], Marcus A. Mall [k,l,m], Loredana Casalis [b], Sarah Köster [d,e], Frauke Alves [c,d,i,n], Giuliana Tromba [b], Christian Dullin [b,c,i,j,*]

[a] University of Trieste, Department of Physics, Via Alfonso Valerio 2, Trieste, 34127, Italy
[b] Elettra Sincrotrone Trieste S.C.p.A., s.s. 14 km 163, 500 in Area Science Park, Basovizza, 34149, Italy
[c] Translational Molecular Imaging, Max-Plank-Institute for Multidisciplinary Sciences, Hermann-Rein-Straße 3, Göttingen, 37075, Germany
[d] Cluster of Excellence "Multiscale Bioimaging: from Molecular Machines to Networks of Excitable Cells" (MBExC), Robert-Koch-Str. 40, Göttingen, 37075, Germany
[e] Institute for X-ray Physics, University of Göttingen, Friedrich-Hund-Platz 1, Göttingen, 37077, Germany
[f] Interdisciplinary Institute for Neuroscience, University of Bordeaux-UMR 5297 and CNRS, 146 Rue Léo Saignat, Bordeaux, 33000, France
[g] University of Trieste, Department of Architecture and Engineering, Via Alfonso Valerio 6/1, Trieste, 34127, Italy
[h] Faculty of Engineering and Health, University of Applied Sciences and Arts, Göttingen, 37085, Germany
[i] Institute for Diagnostic and Interventional Radiology, University Medical Center, Göttingen, 37075, Germany
[j] Diagnostic and Interventional Radiology, University Hospital Heidelberg, Heidelberg, Germany
[k] Department of Pediatric Respiratory Medicine, Immunology and Critical Care Medicine, Charite - University Hospital Berlin, Berlin, 13353, Germany
[l] German Center for Lung Research (DZL), associated partner site, Berlin, Germany
[m] Berlin Institute of Health at Charité – Universitätsmedizin Berlin, Berlin, 10117, Germany
[n] Department for Haematology and Medical Oncology, University Medical Center, Göttingen, 37075, Germany

ARTICLE INFO

ABSTRACT

Pulmonary fibrosis (PF) is a severe and progressive condition in which the lung becomes scarred over time resulting in pulmonary function impairment. Classical histopathology remains an important tool for micro-structural tissue assessment in the diagnosis of PF. A novel workflow based on spatial correlated propagation-based phase-contrast micro computed tomography (PBI-microCT), atomic force microscopy (AFM) and histopathology was developed and applied to two different preclinical mouse models of PF - the commonly used and well characterized Bleomycin-induced PF and a novel mouse model for progressive PF caused by conditional Nedd4-2 KO. The aim was to integrate structural and mechanical features from hallmarks of fibrotic lung tissue remodeling. PBI-microCT was used to assess structural alteration in whole fixed and paraffin embedded lungs, allowing for identification of fibrotic foci within the 3D context of the entire organ and facilitating targeted microtome sectioning of planes of interest for subsequent histopathology. Subsequently, these sections of interest were subjected to AFM to assess changes in the local tissue stiffness of previously identified structures of interest. 3D whole organ analysis showed clear morphological differences in 3D tissue porosity between transient and progressive PF and control lungs. By integrating the results obtained from targeted AFM analysis, it was possible to discriminate between the Bleomycin model and the novel conditional Nedd4-2 KO model using agglomerative cluster analysis. As our workflow for 3D spatial correlation of PBI, targeted histopathology and subsequent AFM is tailored around the standard procedure of formalin-fixed paraffin-embedded (FFPE) tissue specimens, it may be a powerful tool for the comprehensive tissue assessment beyond the scope of PF and preclinical research.

---

* Corresponding author at: Institute for Diagnostic and Interventional Radiology, University Medical Center, Göttingen, 37075, Germany.
E-mail address: christian.dullin@med.uni-goettingen.de (C. Dullin).
URL: https://radiologie.umg.eu/en (C. Dullin).

1. Introduction

Idiopathic pulmonary fibrosis (IPF) is the most common and also one of the most severe forms of progressive pulmonary fibrosis (PF). Patients suffer from chronic shortness of breath, decline of pulmonary function and ultimately death due to respiratory failure 2–3 years after diagnosis, which is comparable with advanced stages of lung cancer. It is expected that the prevalence increases in the future as a consequence of the COVID pandemic [1]. Diagnosis of PF is generally based on the identification of symptoms, medical imaging, lung function tests and in some cases on histopathologic tissue analysis, when invasive lung biopsies were performed. Curative therapeutic approaches for PF treatment are currently lacking. Novel approaches, such as Pirfenidone and Nintedanib [2], aim at prolonging patient survival by slowing down the progression of the disease and to prevent exacerbations. The wide variety of etiological factors that causes PF suggests that different pathomechanisms are involved. A more detailed characterization of fibrotic tissue resulting from various causes in terms of fiber composition, fiber orientation and micro-mechanical properties could improve our understanding of the underlying pathophysiology and may support the development of novel PF treatments. Since structural and functional features cannot be addressed by one analytic method alone, a multi-modal approach is required. In such an approach, typically different parts of the tissue are analyzed by a variety of techniques, each with their own distinct preprocessing steps. Especially in PF, where tissue abnormalities are typically heterogeneously distributed in the lung, spatial correlation of all findings is key for a comprehensive in depth characterization of the disease.

Here a multi-modal analysis pipeline is presented, designed around classical histopathology using formalin-fixed paraffin-embedded (FFPE) tissue specimen. Propagation-based phase-contrast micro computed tomography (PBI-microCT) was employed for the 3D assessment of the whole specimen/whole lung, to target histopathology and for subsequent spatial correlation of the acquired data.

Classical histology, the analysis of thin tissue sections which are subsequently colored using specific staining protocols and the acquisition of images with a standard light microscope, is the most widely used method in both clinical routine and biomedical research. Countless staining protocols are established that allow targeting specific tissue components or cells. Histology, however, has several disadvantages: (i) for the sectioning process the tissue must be embedded in a stiff matrix such as paraffin, (ii) sectioning is performed in a blind manner which does not allow targeting certain regions of interest, (iii) the sectioning can mechanically introduce deformations, (iv) the specimen is destroyed during the sectioning process, and (v) information are intrinsically two-dimensional (2D). In histology, picrosirius red staining is a classical protocol to mark extra-cellular matrix (ECM) components in order to identify fibrotic regions, especially in diseases causing the deposition of connective tissue during tissue remodeling such as PF [3].

Pre-clinical mouse models serve as important tools to investigate the pathogenesis, to establish diagnostic techniques and therapies for PF [4]. The generation of PF by the induction with Bleomycin is the most common PF animal model. Exposure of mice to Bleomycin leads to an initial inflammatory response which is followed by a temporary fibrotic tissue remodeling and resolves within weeks [5]. The translatebility of the results obtained in the Bleomycin-induced PF mouse model into the clinic is heavily disputed [6]. Several treatment approaches that have been found to reduce fibrosis in the Bleomycin-induced PF mouse model have failed in patients [6]. Thus, different PF mouse models like the gentic conditional Nedd4-2 KO mouse model [7–9] are of great interest. The conditional Nedd4-2 KO mouse shows spontaneous and progressive development of PF which is strikingly different from the Bleomycin induced PF model [7]. In the Nedd4-2 model chronic lung disease is induced by means of the deletion of the ubiquitine ligase Nedd4-2 (Nedd4L). This pathology showed common features with IPF, such as honeycombing, alteration in the lung proteome, and increased expression of MUC5B in peripheral airways. Genetic studies suggest that excessive production of the airway mucin MUC5B in lung epithelial cells associated with epithelial remodeling and impaired mucociliary clearance in peripheral airways may be an important trigger of PF [10]. Thus, the two different PF models (Bleomycin induced and the conditional Nedd4-2 KO) due to their different pathomechanisms, may develop characteristically different fibrotic features. Therefore, they allow studying the sensitivity of the here developed analysis pipeline based on its ability to discriminate between those models.

The analysis of PF by for instance histology is typically hindered by the fact that PF causes heterogeneous and patchy alterations within the lungs. Thus, to identify fibrotic sites phase contrast microCT – a technique developed in the middle of 1990s – is ideally suited as it allows studying whole lungs. During the years, PBI-microCT has been applied in different research fields, such as material science [11], cultural heritage [12], and plant research [13]. However, one of the most successful applications of this technique is label free (without additional contrast agents) biomedical imaging, especially targeting soft tissue (composed by materials with a $Z < 10$). Unlike, classical absorption based microCT, which exploits differences in the attenuation of x-rays as they pass through the sample, in phase-contrast microCT interference effects caused by phase shifts of the x-rays at tissue interfaces are recorded as well. Optical properties of tissues can be characterized by their refractive index. In its complex form it can be expressed as $n = 1 - \delta - i\beta$, where δ and β represent the phase shift and absorption properties of the tissue respectively. For medical applications, the photon energy is in the range of 10–200 keV. In this interval, the real part of the refractive index is roughly three orders of magnitude larger than the imaginary part for soft-tissue, rendering the phase effects more important than attenuation. However, in order to exploit this technique, some conditions need to be fulfilled: (i) spatial coherence, (ii) a sample-to-detector distance much longer than used in classical microCT, as well as (iii) a high resolution detector to resolve the interference fringes.

Since conventional x-ray tubes are incoherent, typically synchrotron facilities are exploited for phase contrast imaging as they generate x-rays with a high level of coherence. A further advantage is, that synchrotrons provide a very high flux, which allows decreasing the scanning time of a specimen dramatically [14]. Saccomano et al. [15] showed that PBI-microCT as utilized in this study is highly suited to image paraffin embedded specimens without the need of additional contrast agents. Albers et al. [16] demonstrated that this approach can be used to supplement classical histology with 3D structural information, while not interfering with subsequent cutting and staining of the specimen [17]. Since PBI-microCT is typically fast, larger specimens like an entire FFPE tissue block can be imaged in total in a mosaic approach at a resolutions of few micrometer.

However, a big disadvantage of PBI based label-free virtual histology of paraffin embedded tissue is the lack of specific tissue contrast. Nevertheless, it has been demonstrated that apparent changes in the anatomical structure e.g. in lung tissue can successfully be used to localize fibrotic regions and to estimate the severity of PF [18]. Since ECM fibers, such as collagen, do not provide enough contrast to be distinguished from other tissue structures a combination of structural imaging by, for instance, the means of PBI-microCT with tissue specific techniques such as classical histology is of great interest to characterize fibrotic processes.

In the development of PF the elastin is replaced by collagen fibers, which are less elastic and decrease the compliance of the lung [19]. Therefore, the evaluation of the changes in the mechanical properties, especially the stiffness, of the tissue, that can be achieved by means of Atomic Force Microscopy (AFM), may play a crucial role in our understanding of PF pathophysiology. AFM, a scanning probe microscopy technique invented in the 1980s, is a very versatile and powerful tool allowing force measurements [20], topographic imaging [21] and manipulation [22]. The AFM set up comprises a piezoelectric transducer,

a laser, a mirror, and a photodiode that are housed in the so-called "head" of the AFM. A cantilever is inserted inside the head, that is then placed over the sample. Here the force measurement was used in which the tissue was locally probed with the cantilever. The deformation of the cantilever and the intention force is recorded and in combination with the known mechanical properties of the cantilever allow the calculation of the local stiffness typically expressed as Youngs modulus (E). The development of fibrosis is associated with a deposition of ECM components resulting in a higher amount of fibers compared to the homeostasis condition, leading to changes in the mechanical properties. In lungs, these structural modifications cause a stiffening of the tissue. Calò et al. [23] reported that specifically stained tissue sections to highlight fibers such as collagen, can be used as a reference map for the correlative biomechanical characterization of the tissue via AFM.

Therefore the aim of this study was to integrate structural and mechanical features from hallmarks of fibrotic lung tissue remodeling, using a combination of propagation-based phase-contrast micro computed tomography imaging (PBI-microCT), atomic force microscopy (AFM), and classical histology and evaluate the prognostic value of such an approach by comparing two mouse models in which PF is induced by different means. A further aim of this study was to demonstrate how local measurements such as AFM can be integrate into a larger 3D context such as a PBI scan of an entire FFPE tissue block.

2. Material and methods

2.1. Ethical statements

Animal procedures were performed in compliance with the guidelines of the German ethical laws, were approved by the administration of Lower Saxony, Germany (approval number G17.2585) or University of Heidelberg (Regierungspräsidium Karlsruhe, Karlsruhe, Germany) (approval number 35-9185.81/G-45/14) and are reported in accordance to the ARRIVE guidelines (https://arriveguidelines.org).

2.2. Animal models and sample preparation

Two different mouse models, Bleomycin induced (PF_{ble}, N = 6) and the conditional Nedd4-2 KO model (PF_{gen}, N = 16) [7] both developing PF were investigated. In the first model, PF was induced in 8 adult male BL6 mice by intra-tracheal instillation of 1.5 mg Bleomycin in a volume of 50 µl of 0.9% sodium chloride solution [24]. In two of these mice, one week after induction of PF, 60 mg/kg of Nintedanib dissolved in 200 µl 1% Tween 80-PBS was administered via oral gavage daily until day 21 to mitigate the development of PF ($PF_{ble} + Nin$, N = 2). Mice for conditional deletion of Nedd4-2 in lung epithelial cells were generated by intercrossing Nedd4-2^fl/fl, CCSP-rtTA2S-M2, and LC1 mouse lines, all on a C57BL6/N background, as previously described [7]. Nedd4-2^fl/fl littermates served as controls. Mice were housed in pathogen-free conditions with free access to food and water. Nedd4-2 deletion was induced using doxycycline hydrochloride (Sigma) in 5% sucrose water starting at the age of 4–6 weeks. Furthermore, lung specimens of 16 adult female/male conditional Nedd4-2 KO mice [7] were analyzed. Lungs from a total of nine age matched mice, three healthy controls from the Bleomycin model (CN_{ble}, N = 3) and six healthy mice from Nedd4-2 (CN_{gen}, N = 6), were used as controls. For more details, please refer to Table 1. Since no differences and a low variation in the controls were expected a relatively low number of mice were used in those groups. Bleomycin induced PF is a very standardized method, however with severe side effects, thus less mice than of the genetic model were utilized. The two Nintedanib treated mice presented a proof-of-concept application for the developed pipeline.

After sacrificing the mice by cervical dislocation, lungs were harvested. In case of the Bleomycin model lung were filled and fixed in formalin, dehydrated using an ascending ethanol series and then embedded in paraffin as described previously [25]. Following in-situ

Table 1
Overview of the different animal models used. Values are displayed as mean ± standard deviation.

Experimental group	# of mice	Weight [g]	Age [d]
Healthy controls (CN_{ble})	3	25.0 ± 1.0	186.8 ± 44.5
Bleomycin (PF_{ble})	6	14.1 ± 1.7	97.5 ± 4.0
Bleomycin + Nintedanib ($PF_{ble} + Nin$)	2	19.4 ± 3.3	100.0 ± 1.4
Control of genetic model (CN_{gen})	6	29.8 ± 3.6	174.0 ± 13.4
Nedd4-2 KO (PF_{gen})	16	27.8 ± 4.1	183.1 ± 37.7

ex-vivo microCT, the lungs from the conditional Nedd4-2 KO model as well as from the respective controls were harvested, filled with air and fixed in formalin and then processed in the same way as the lungs of Bleomycin model.

2.3. Propagation based imaging (PBI)

All specimens were scanned at SYnchrotron Radiation for MEdical Physics (SYRMEP) beamline of the Italian synchrotron "Elettra" Trieste, Italy [26]. The acquisitions were performed using the white beam setup in propagation-based phase contrast modality (PBI), with a sample-to-detector distance of 150 mm. The beam was filtered with a silicon foil of 0.5 mm thickness, resulting in a mean x-ray energy of 16 keV. 360° off-center scans with 3600 projections, and an exposure time of 50 ms per projection, were performed using a water-cooled Orca Flash 4.0 sCMOS detector (2048 × 2048 pixels) coupled with a 17 µm thick Gallium Gadolinium Garnet (GGG) scintillator. The reconstructed pixel size was 2 µm, resulting in a reconstructed field-of-view of roughly 7 × 4 mm². To capture most of the lung tissue, about 2 to 3 scans were performed with a vertical offset of 3.5 mm. Before the reconstruction using the filtered back-projection algorithm, the Paganin's phase retrieval algorithm [27] was applied with a δ/β ratio of 100 both implemented in the SYRMEP Tomo Project (STP) software [28]. For each sample, the vertical steps were stitched together using an in-house Python script.

2.4. Histology

For all specimen, the position of fibrotic regions of interest (depth from the paraffin surface) was calculated in the PBI data sets using VGSTUDIO MAX. Then, from each block, a targeted slice of 5 µm was cut with a microtome, fixed on a glass plate, deparaffinized and subsequently stained with picrosirius red as described before [3]. An Axioskop 2 (Carl Zeiss Microscopy GmbH, Jena, Germany) microscope in combination with a Leica DC 100 camera (Leica, Switzerland) as well as an Axiovert 200 inverted microscope (Zeiss) were exploited. To depict the whole lung sections, the built-in stitching algorithm of the microscope was applied in combination imaging tiles at a 10× magnification. For determination of the extent of PF in each lung section the Ashcroft scoring system [29] with a score ranging from 0 up to 8, where 0 corresponds to healthy lung tissue and a score of 8 is assigned to severe PF. Three independent readers scored each slice in a blind manner, selecting three regions per slice and three slices per sample. The fibrosis score for each lung was taken as the median value of all the scores.

2.5. Atomic force microscopy (AFM)

For all specimen, a targeted slice of 5 µm was cut adjacent to the ones used for histology and deposited on a slice of Calcium Fluoride (CaF₂). After that, the tissue slice was deparaffinized and re-hydrated using the following protocol: 1 h in the oven at 65°, 15 min in Xylol, a quick wash in fresh Xylol, 10 min in Ethanol 99%, 10 min in Ethanol 96%, 5 min in Ethanol 50%, transferred in water for the measurement. The AFM measurements were carried out at Georg-August-University
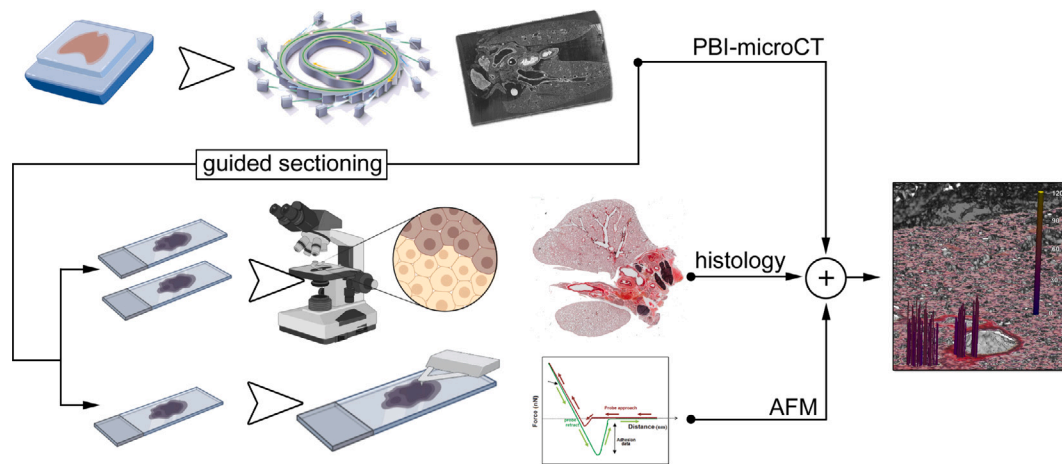
Fig. 1. Graphical illustration of the presented pipeline. Whole FFPE mouse lungs were scanned with PBI at the SYRMEP beamline of the Italian synchrotron, resulting in a 3D representation of the entire specimen (first row) which allowed screening and identification of planes of interest. Subsequently, the specimens were sectioned. Adjacent sections were used for classical histology (second row) and AFM (third row). The results were then fused using elastic registration which resulted in spatial integration of the information into a single data set.

Göttingen, Institute for X-ray Physics with Nanowizard 4 (JPK, Bruker Nano GmbH, Berlin, Germany), on an inverted light microscope (IX73; Olympus, Tokyo, Japan) with a 20x objective (LUCPlanFLN, NA = 0.45, Olympus) in force spectroscopy mode, with a set point of 10 nN, Z speed of 2 μm/s using a pre-calibrated cantilever (SiO_2) with a spring constant of 0.062 N/m and a bead of 2.5 μm diameter (Novascan Technologies, US). All measurements were performed in water. JPK Data Preprocessing software (version 7.0.165, Bruker Nano GmbH, Berlin, Germany) was used to retrieve the Young's moduli. For all the force curves a baseline subtraction and contact point determination were applied before performing the elasticity fit of the curve. A histological lung section, taken 5 μm above the one measured with the AFM, was used as a reference map for the identification of the region of interest (ROI) in the lung.

2.6. Software

SYRMEP Tomo Project (STP) 1.6 [28] was used to perform the reconstructions. Python 3.8 was used to perform the vertical stitching of the 3D reconstructed volumes, the registration of the force measurements performed with AFM and the optical images, and all the plots. To perform the vertical stitching Python3 in combination with the following modules was used: numpy 1.22.2, matplotlib 3.6.2, and scikit-image 0.19.1. For the registration of the force measurements Python3 in combination with numpy 1.24.3, matplotlib 3.7.1, Pillow 9.5.0, zipfile, os, skimage 0.21.0, and pandas 2.0.1 was applied. To generate the box plots and the statistical analysis, the following Python packages were used: utils version 1.0.1, pandas version 2.0.1, seaborn version 0.11.2, matplotlib version 3.7.1, statannotations version 0.5.0, scipy version 1.9.2. VG STUDIO MAX 3.1 was utilized to carry out the morphological analysis of the 3D stitched volumes as well as to render the spatial correlated PBI, histology, and AFM data sets. Photoshop 2023 was applied to correct for global rotation angles before the application of elastic registration performed with Fuxlastix [17]. Fiji was used to stitch images of the picrosirius stained lung sections obtained in combination with a polarization filter, as well as for converting the output of Fuxlastix to TIF-format. JPK Data Processing (DP) was used to fit the force curved acquired with the AFM.

2.7. Statistics

Statistical analysis was done with the Python3 packages statannotations and scipy. Pairwise none-parametric Mann–Whitney U test are presented with $p > 0.05$ = ns (none significant), $p \leq 0.05$ = *, $p \leq 0.01$ = **, $p \leq 0.001$ = ***, $p \leq 0.0001$ = ****. All presented box plots are generated with the seaborn python package. The box represents the range between the 25th and 75th quartile showing the median as additional line in between. The whiskers extend to 1.5 times the interquartile range. Everything outside that range is considered an outlier and displayed as individual data point.

3. Results

3.1. Pipeline design

A correlative pipeline for FFPE lung tissue imaging and analysis was implemented. The same unmodified approach of tissue fixation and paraffin embedding which is used in standard pathological tissue analysis in clinical routine was applied.

First, all paraffin embedded lung specimens were scanned using the white beam PBI setup at the SYRMEP beamline of the Italian synchrotron, resulting in a 3D representation of virtually the entire lung specimen at 2 μm isotropic spatial resolution. The reconstructed dataset was used to screen the entire tissue block and identify fibrotic regions of interest. Subsequently, targeted microtome sectioning was performed and adjacent 5 μm thick lung slices from predefined levels in the tissue block were obtained for histology and AFM. Using elastic image registration, the resulting light microscopic images as well as the AFM data were integrated into the 3D context of the PBI data set by utilizing the online microscopy image of the AFM device as reference.

The same paraffin embedded lung tissue was successfully analyzed in all three image modalities. This allowed correlating 3D anatomical alterations seen in PBI, with specific cell- and ECM components as fibers visualized in histology as well as the spatial integration of local impact on local tissue stiffness as measured by AFM. The entire pipeline is sketched in Fig. 1.

3.2. Structural changes in PF are revealed by morphological analysis using PBI-microCT

Due to the heterogeneity of PF throughout the entire lung, analysis was performed in volumes of interest of the size of $300 \times 300 \times 300$ μm. Eighteen of these regions were placed in each PBI-microCT data set avoiding larger structures such as bigger bronchi or vessels. Six cubes were placed in the fibrotic region (if present), six cubes were placed in a morphologically non-affected region and the last six were positioned at the interface of fibrotic and healthy regions. Fig. 2a shows four
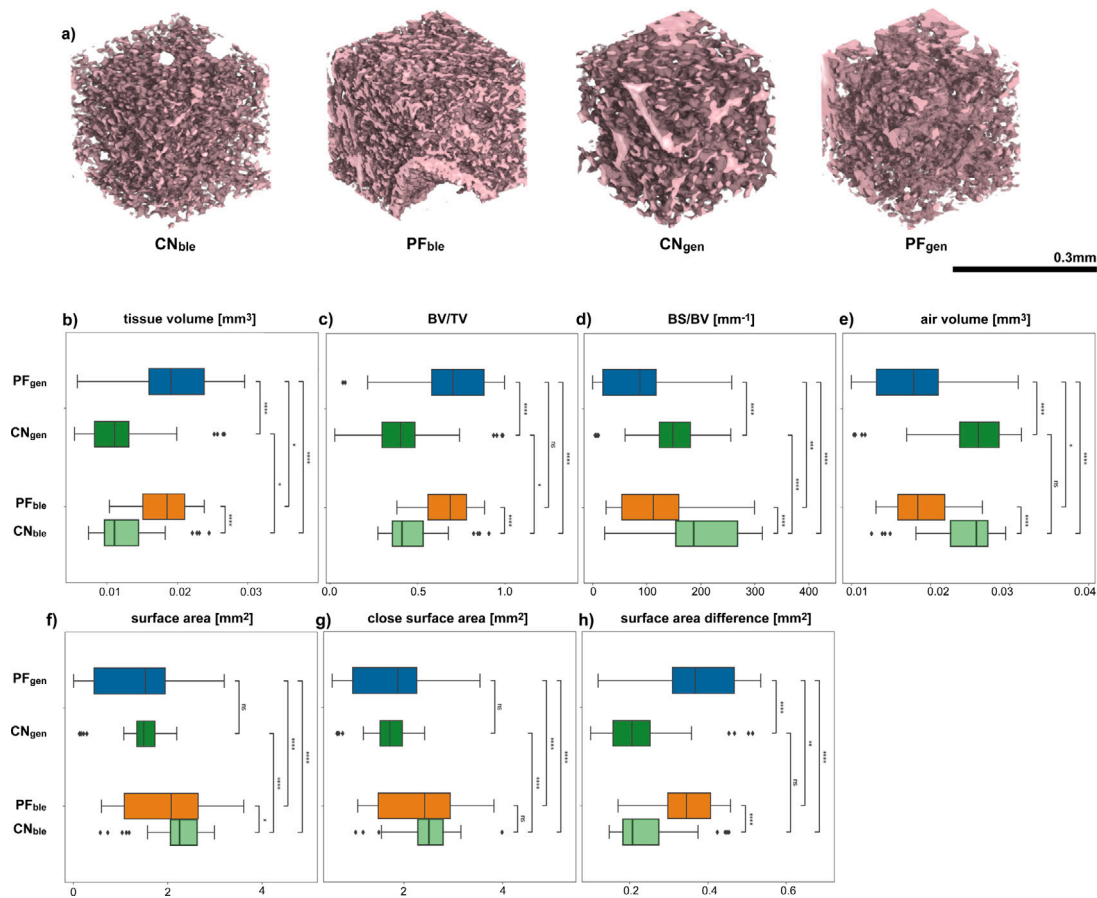
Fig. 2. Quantification of structural alterations in lungs with PF. (a) Representative 3D-illustrations of $300 \times 300 \times 300$ μm^3 analysis cubes from CN_{ble}, PF_{ble}, CN_{gen}, and PF_{gen}. Clearly, a reduction of the active surface and an increase in tissue volume is seen in both cases of PF, however, much stronger in PF_{ble} lungs. (b)–(h) shows the quantification results for different parameter. Both groups of mice with PF express a larger lung tissue volume (b) and a reduced air volume (e). Interestingly, the surface area (as well as the closed surface area) does not show strong deviations from the respective controls (f and g). The body surface to body volume ratio (BS/BV) presenting the normalized surface of the lung tissue expressed the expected reduction in both mice models of PF, with a stronger tendency in PF_{gen} mice (d). This points to a reduction in the functional capability of the PF lungs and also to stronger severity of the PF in PF_{gen}. For each mouse 6 cubes were analyzed taken from 16, 6, 8, and 3 numbers of animals for PF_{gen}, CN_{gen}, PF_{ble} and CN_{ble} respectively.
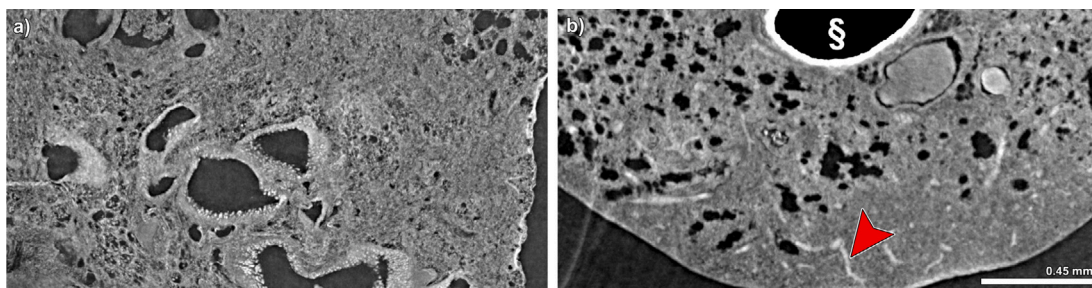
Fig. 3. Maximum intensity projections (0.02 mm thickness) of the PBI-microCT data of (a) a PF_{ble} mouse and (b) a PF_{gen} mouse show, in the same magnification, differences in the consolidated lung regions. While in PF_{ble} the consolidated regions seem rather homogeneously dense (a), in PF_{gen} additional dense structures (most likely vessels) are visible (red arrow head) (b). Note: §indicates an air bubble in the paraffin block trapped in a major airway.

examples of such cubes for lungs of (i) CN_{ble}, (ii) PF_{ble}, (iii) CN_{gen} and (iv) PF_{gen}. A threshold was manually adjusted in order to extract the surface of the lung tissue. Then several parameters were calculated: tissue volume, air volume (more precisely the volume of the paraffin filled air spaces), surface area, closed surface area, surface area difference, body volume/total volume (BV/TV), and body surface/body volume (BS/BV), which are summarized in Fig. 2 (b)–(h). Tissue volume presents the accumulated volume of all structures within the cube, which had a intensity above the selected threshold. Air volume is calculated as total cube volume minus tissue volume. Thus, in case of fibrosis the tissue volume will increase and the air volume decrease.

Since the measurement cubes artificially cut the lung tissue, the surface of the lung tissue was measured either ignoring the cut faces of the measurement cubes (surface) or including the cut faces (closed surface). Moreover, the difference between both was calculated, which was higher for larger objects intersecting the measured regions. In addition, the tissue volume ratio (BV/TV) and the surface were normalized by the tissue volume (BS/BV). The lung tissue volumes (0.019 ± 0.005 mm^3 and 0.018 ± 0.003 mm^3 for the PF_{gen} and PF_{bleo} respectively) in the fibrotic lung models appear significantly enlarged compared to their control groups (0.011 ± 0.004 mm^3 and 0.012 ± 0.004 mm^3 for the CN_{gen} and CN_{bleo} respectively), Fig. 2(b). As shown in Fig. 2 this results
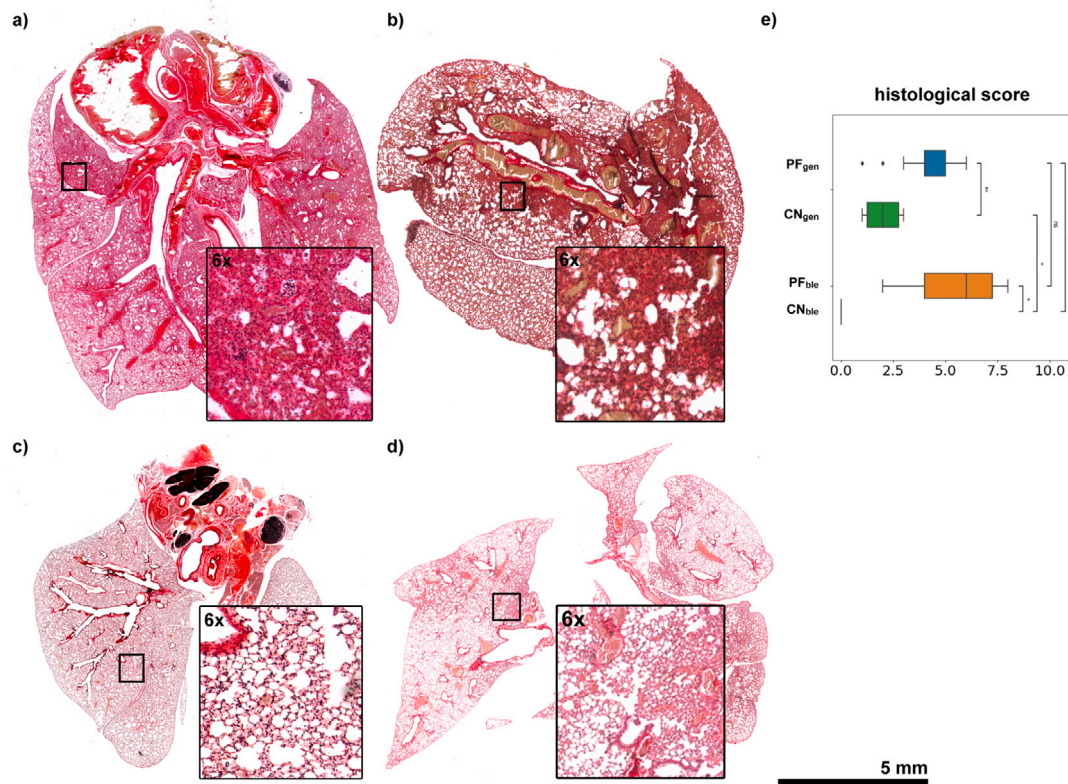
Fig. 4. Quantification of PF using histological scoring. (a)–(d) shows picrosirius stained lung section obtained from a PF_{ble}, a PF_{gen}, a CN_{ble} and a CN_{gen} mouse. The severity of the fibrotic consolidations were scored in 3 regions randomly distributed over the entire slice. (e) presents the histological score for each group. [score example (a) = 8, (b) = 6, (c) = 0, (d) = 3].

in a significant reduction of the relative surface area (BS/BV) (Fig. 2d). While the difference in the lung tissue volume between PF_{gen} and PF_{ble} was rather small, the difference in BS/BV (86.01 $\pm$ 62.00 mm^{-1} and 118.60 $\pm$ 70.00 mm^{-1} for the PF_{gen} and PF_{bleo} respectively) was a bit larger (Fig. 2b and d). However, since lungs of the control groups revealed the same difference in BS/BV (147.73 $\pm$ 50.70 mm^{-1} and 200.00 $\pm$ 74.70 mm^{-1} for the CN_{gen} and CN_{bleo} respectively), it can be assumed that this tendency was attributed to differences in sample preparation. This is further illustrated in Fig. 3 showing clear differences in the substructures of the consolidated regions of lungs from in Fig. 3(a) a PF_{ble} mouse in comparison to Fig. 3(b) a PF_{gen} mouse. In summary, lungs of both PF mouse models consist of regions of tissue with consolidation to roughly the same extent. However, the substructures of the regions appeared to be different. In PF_{gen} the consolidated area showed dense substructures (red arrow in Fig. 3) which most likely represent vessels while in PF_{ble} the consolidated areas appeared homogeneous.

3.3. Quantification of PF by histological scoring

Histological assessment of PF was performed on all lung specimens by applying the Ashcroft scoring system [29] to picrosirius red stained histological lung sections. Fig. 4 shows examples of a PF_{ble} lung (a), a PF_{gen} lung (b), a CN_{ble} and (d) a CN_{gen} lung (c). Clearly, in both PF_{gen} and PF_{ble} dense regions, heterogeneously distributed throughout the lung section, can be seen. The comparison of the controls reveals also some denser areas in CN_{gen} compared to CN_{ble} resulting in a average score greater than 0 (2.8 $\pm$ 1.7). Fig. 4(d) demonstrates the scoring results. Here, clearly the PF_{ble} mice were rated to develop more severe PF (5.6 $\pm$ 2.2) than the PF_{gen} mice (3.8 $\pm$ 1.7), in contrast to the PBI results. While each of the PF models have a significantly higher score then there respective controls, in comparison to each other the histological score is not significantly different .

Fig. 5 shows two examples of picosirius stained lung slices imaged with polarized light. In that case orange depicts thick fibers - collagen type I and green thin fibers - collagen type III. Clearly, PF_{ble} lungs (Fig. 5a) show more collagen type I and the PF_{gen} lungs (Fig. 5b) more collagen type III, within the perivascular areas.

3.4. Atomic force microscopy (AFM) measurements of de-paraffinized and re-hydrated paraffin embedded lung tissue sections

To address mechanical changes in the lung tissue due to the depositioned fibers, atomic force microscopy was applied to measure the local Young's moduli of the tissue. In particular, three areas, for the lungs of PF_{gen} and PF_{ble} were selected: perivascular ROIs (collagen deposition), the lung parenchyma, and ROIs of tissue consolidation; whereas for lungs of the CN mice only the first two ROI's were measured, since no consolidation was observed. Fig. 6 (a) and (b) illustrate the positions of the force curve measurements in relation to the online acquired microscopic images (red). To provide a way to display the AFM measurements in a 3D context, the Young's moduli were represented as bars in a 3D data set. Fig. 6(c) shows that this allows to display measurement position and measurement result in relation to the online microscopic image in a 3D context. Fig. 6(d) demonstrates that the Young's moduli were significantly different between the three groups (PF_{gen}, PF_{ble} and CN). Note, that since no differences were found between CN_{ble} (54.7 $\pm$ 15.9 kPa and 52.8 $\pm$ 14.9 kPa for the perivascular and the parenchymal regions, respectively) and CN_{gen} (61.6 $\pm$ 14.5 kPa and 61.7 $\pm$ 15.6 kPa for the perivascular and the parenchyma regions, respectively), they were pooled to one group (CN). The results show the highest Young's moduli for the lungs of the PF_{gen} (96.8 $\pm$ 28.5 kPa, 112.2 $\pm$ 21.3 kPa, and 106.6 $\pm$ 23.2 kPa for the perivascular, the parenchymal, and the consolidation regions, respectively) group, followed by the PF_{ble} model (74.9 $\pm$ 17.6 kPa, 75.9 $\pm$ 20.3 kPa, and
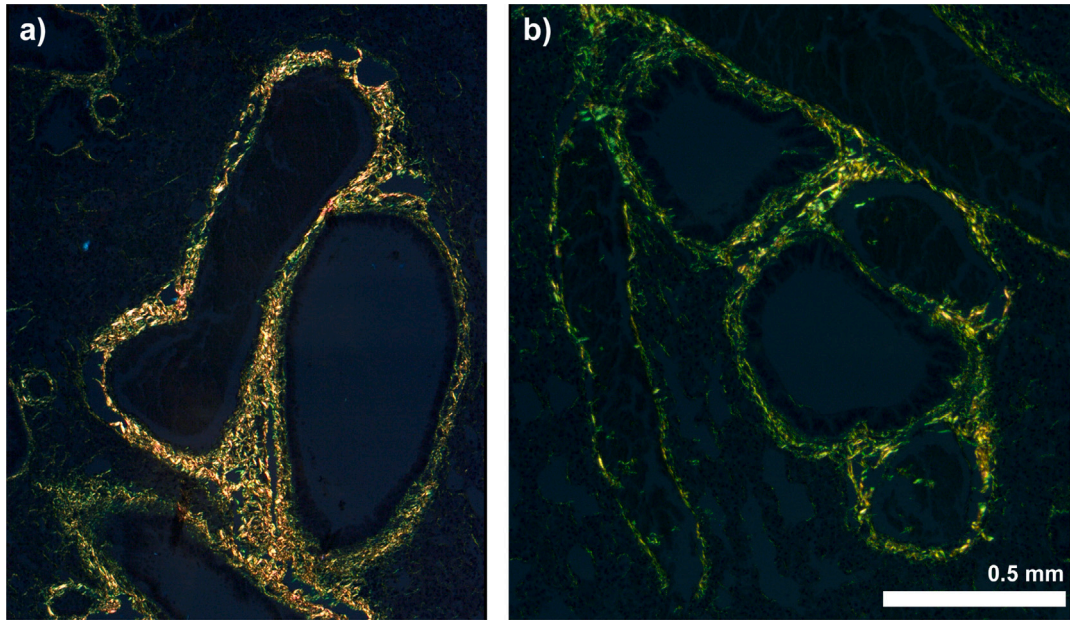
Fig. 5. Picosirus stained lung sections imaged with polarized light of a (a) PF_{ble} mouse and (b) a PF_{gen} mouse. An orange color depicts a higher accumulation of collagen-Typ-I, whereas green is an indication of a higher collagen-Typ-III content.
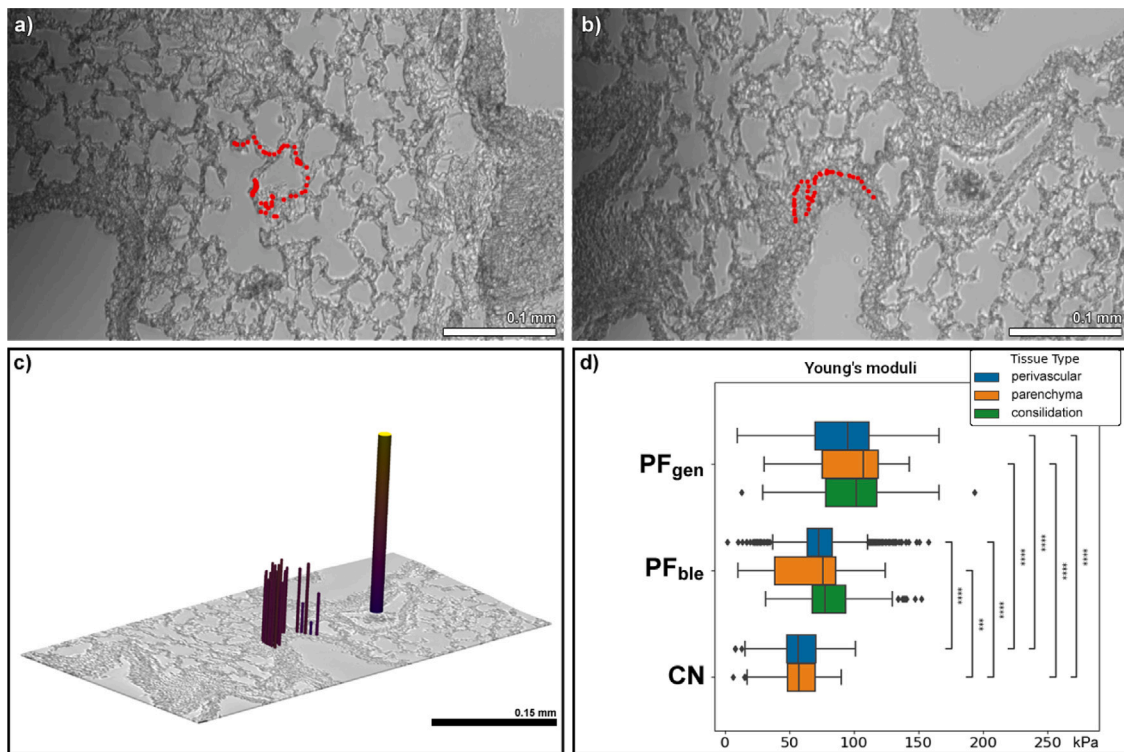

Fig. 6. AFM measurements. (a) and (b) show example positions of the AFM measurements (red dots) for lung parenchyma and a region of perivascular fiber depositions in a CN lung, respectively. The obtained Young's moduli were then mapped into a 3D bar plot in order to render it into the 3D context of the CT data. (d) depicts the results of the AFM measurement. CN_{ble} and CN_{gen} were condensed to one group CN. Measurements were performed in three ROI's per one slice per specimen (perivascular (blue), lung parenchyma (orange), visually consolidated area (green). For each model sections of 3, 5, 8 mice for PF_{gen}, PF_{ble} and CN respectively, were measured.
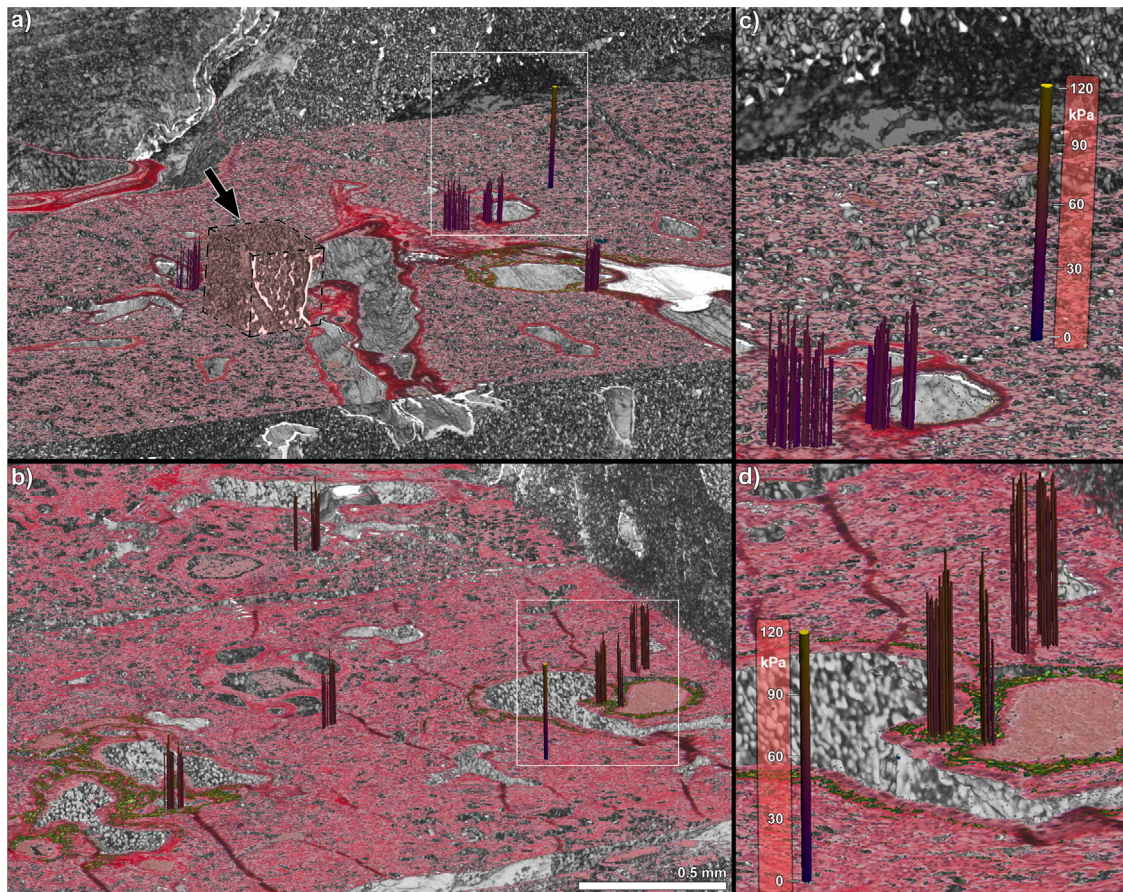
Fig. 7. 3D integration of PBI, histology and AFM. (a) and (b) show the 3D registration results of a CN_{ble} and a PF_{ble} mouse respectively. Clearly, the latter lung appears more dense. Nevertheless also healthy areas like in the upper part of the image are visible. In (a) a cube is presented to demonstrated the region covered for one measurement in the structural analysis. On top of the Picrosirius stained slices, locally histological images obtained in combination with a polarization filter (green/yellow) are shown to validate that the observed structures are indeed collagen fibers. Moreover, the locations of the AFM measurements are depicted as well including a scale bar. In the close-ups (c) and (d) it becomes apparent that the stiffness in the PF_{ble} lung was found higher than in the CN_{ble} lung in both perivascalur and parenchyma regions.

79.1 ± 20.8 kPa for the perivascular, the parenchymal, and the consolidation regions, respectively). Interestingly, no huge differences were found in obtained values of the Young's moduli between the three different anatomical regions/ROI's.

3.5. Spatial correlation using elastic registration

For the spatial correlation between PBI-microCT, histology and AFM, several pre-processing steps were required. First, the 3D volume acquired with PBI-microCT had to be re-oriented to match the cutting direction of the histological workflow. Second, the 3D PBI volume data set was cut virtually and the cutting plane was rotated until it matched roughly the orientation of the histological image. Since cutting with a microtome is known to introduce deformations in the generated tissue section, those cannot be directly overlaid with the PBI-microCT data. Thus, elastic image registration between the histological lung section and corresponding virtual cutting plane in the PBI-microCT was applied using the Fuxlastix software [17]. This step produced a new histological image with compensated deformations. Subsequently, this modified histological lung section was used as 'fixed' image for a second elastic registration with the online microscopic image of the AFM measurement. The calculated transformation was then applied to the measured Young's moduli after they were converted into a 3D matrix as described above. This pipeline allowed to spatially correlate both the histological lung sections and the AFM measurements into the 3D context of the PBI-microCT data sets.

Fig. 7(a) and (b) show representative examples for a CN_{ble} and a PF_{ble} lung, respectively. The depicted CN_{ble} lung displayed no dense

regions, and the lung parenchyma appeared regular. The Bleomycin-induced fibrotic lung tissue was found more dense and displayed large consolidated regions. The elastic transformation performed on the histological images resulted in a perfect match with the PBI-microCT data set. No apparent discontinuities between the 3D lung tissue in PBI and the histological section were found. In Fig. 7a) also an example of a cube used for the porosity evaluation of the tissue is displayed to provide a visual reference for the areas covered by this analysis. Fig. 7(c) and (d) show magnifications of the two areas (collagen deposition areas) of the CN_{ble} and PF_{ble} lungs, respectively (indicated by the white rectangles in (a) and (b)). In these two mentioned areas, biomechanical measurements were performed, and the results, in terms of stiffness (Young's modulus (kPa)) are displayed as bars. The height of the bars, so the stiffness, was roughly twice as high in the PF_{ble} example compared to the CN_{ble} control. Furthermore, in Fig. 7(d), the visible green and yellow stained regions presents the registration of a Picrosirius stained section also registered to CT and AFM. Green colors depict collagen III and yellow collagen I. In summary, Fig. 7 demonstrates that with the here presented pipeline, results from PBI, histology, and AFM can precisely be co-registered, allowing putting all subsequently generated data (histology and AFM) into the correct 3D local environment.

3.6. Cluster analysis of the obtained features

Hierarchical clustering was performed using the combined data collected from the morphological analysis and the biomechanical measurements. From the structural PBI based analysis the average lung

tissue surface (surface are), the closed lung tissue surface area (closed surface area) as well as their difference (Δsurface area) were used in combination with the tissue volume (tissue volume), the relative tissue volume (BV/TV) and the tissue surface normalized by the tissue volume (BS/BV). From the AFM measurement the average Young's moduli from the para-vascular region (E vessel) and the lung parenchyma (E parenchyma) were used. The stiffness of the consolidated areas was excluded as it was not measured in the control specimen. Fig. 8 shows the calculated clustermap. In order to give each feature x the same impact on the clustering result the each individual values x_i were converted into the so-called z-score z_i, according to:

$$z_i = \frac{x_i - \mu}{\sigma}, \text{ with } \mu = \frac{1}{N} \sum_i (x_i), \sigma = \sqrt{\frac{1}{N} \sum_i (x_i - \mu)^2}$$

The resulting values are denoted in the cells of the clustermap. Each row presents one individual specimen for which the group assignment is color coded on the left side and the given histological score is stated for comparison on the right side. The histological score was not included in the clustering to demonstrate that specimens of the different experimental groups that share the same histological score are grouped correctly given the additional information provided by the combined measurements. To calculate the clustermap a "complete" linkage and a cosine similarity was used. The latter depicts that the cosine of the angle between two feature vectors defines the similarity. Linkage "complete" means that the distance $d(u, v)$ between two cluster or elements u and v is calculated for all elements u_i and v_j of cluster u and v respectively as:

$$d(u, v) = maxdist(u_i, v_j)$$

Therefore clusters were joined iteratively which had a minimal $d(u, v)$. Looking at the horizontal dendrogram, two clusters are clearly visible at the highest level, successfully separating the fibrotic mice (red and blue, PF_{gen} and PF_{ble}) from healthy and treated mice (green and yellow, CN and $PF_{ble} + Nin$). At the next hierarchy level, the fibrotic lungs are nearly perfectly split into lungs obtained from PF_{gen} and PF_{ble} mice, suggesting significant differences in feature combination in the two models. The vertical dendrogram shows the correlation in between different features. Surface area and closed surface area are highly correlated as well as object volume and Δ surface area. The outcome suggests that the combination of PBI and AFM does allow a comprehensive prediction of the fibrotic state as well as the model.

4. Discussion

Here a novel workflow was presented for the spatial correlation of data obtained by PBI-microCT, histology and AFM measurements of FFPE lung tissue excised from two different mouse models of PF, the classical Bleomycin-induced PF model (PF_{ble}) as well as the conditional Nedd4-2 KO model (PF_{gen}) [7]. After the PBI acquisition of the entire paraffin block, histology and AFM was performed on lung tissue slices. Using elastic registration the deformations of the slicing process were compensated, which resulted in a precise 3D spatial registration of the data of all three imaging methods, allowing to supplement information from one modality with those obtained in the others.

The sensitivity of our approach was validated by its application on two different PF mouse models (Bleomycin induced PF and conditional Nedd4-2 KO). Our results clearly indicate differences in the histological appearance and the mechanical properties between those two models, while on the other hand structural changes such as the extent of consolidated areas, as evaluated by PBI, were pretty comparable. The PF_{gen} mice presented a higher content of collagen-Typ-III than collagen-Typ-I in contrast to the PF_{ble} model. While the histological score was significantly higher in PF_{ble} - mostly depicting stronger consolidation, the stiffness measured in AFM was lower. This might indicate that the consolidated regions in these two models are differently composed, which in turn could be an indicator that the pathomechanisms causing

the PF are different. Comparison of the two models however was limited to the facts that in the Bleomycin induced model fibrotic regions are typically placed more in the central part of the lung, while in the conditional Nedd4-2 KO model fibrotic sites were found more towards the periphery, which could have biased the analysis. In addition the models have a very different time schedule. In the Bleomycin induced model the induction only takes a few days while in the conditional Nedd4-2 KO model the mice were observed over several month. Thus, the two experimental models were not age matched, which might explain the slightly elevated fibrosis score in the CN_{gen} in which mice were older than the CN_{ble} group. Thus, the observed differences in the experimental groups can only present a first hint of a potential difference between the composition of the fibrotic regions and additional in-depth characterization is required. This also holds true for a future translation of this pipeline to human PF tissue specimen, which hopefully aids to the identification of potential targets for novel PF treatments.

The combination of microCT and AFM has already be proposed for instance by Lartey et al. [30]. However, in this study microCT was only used to identify and isolate lung metastases for subsequent AFM analysis, and no extensive cross modality data registration, in contrast to our approach, was performed. To provide anatomical background to AFM measurements also combinations with other techniques have been proposed such as by Gomez-Varela et al. [31] who presented a setup allowing simultaneous acquisition of AFM and high resolution microscopy such as PALM STORM. Of course the approach remains 2D and depends heavily on the tissue region that has been sectioned before. Thus, the combination with PBI has some promising advantages as it allows to select fibrotic regions in 3D and provides the ability to perform quantification of 3D features as shown in our manuscript.

The presented workflow is not restricted to lung tissue and will work in the same way for all FFPE tissue. Since, no additional treatment of the specimens is required, the workflow can also be applied on archived FFPE tissue which would allow correlating the findings with records of treatment outcomes and survival rates in patients or in other animal studies.

However, it needs to be mentioned that FFPE tissue presents a compromise in the tissue preparation for the used technologies (PBI, histology and AFM). It is been shown by Calo et al. [23] that AFM is more sensitive in fresh or frozen tissue samples then in rehydrated former FFPE tissue. Such an approach would not allow registering the measurements with the data of the other methods. The study of Calo et al. [23] cannot directly be compared to our results as they used thicker sections of 10 μm in comparison to the 5 μm used here. Moreover, the rehydration step is not clearly described in that publication, which renders comparison with our protocol challenging. A further study presented by Anura et al. [32] did also perform AFM on FFPE tissue, in their case on slices of human oral mucosa and correlated the findings with observations in histology. They found significant differences in the Young's moduli between healthy and fibrotic mucosa but they did not provide a spatial correlation with the histology. This suggests that while FFPE tissue is not ideal for AFM still relevant information can be retrieved. Nevertheless, the data suggests that for future spatial registration of PBI, histology and AFM the possibility to apply our pipeline on frozen specimen needs to be evaluated.

5. Conclusion

The established novel workflow for 3D spatial correlation of PBI, histology and AFM on FFPE lung tissue specimens. By applying this workflow in two different models of PF significant differences were found in anatomical alterations and tissue stiffness. Based on this promising results, the presented pipeline might constitute a general approach for correlative assessment of FFPE tissue of any origin. This procedure is compatible with FFPE specimen from diagnostic biopsies
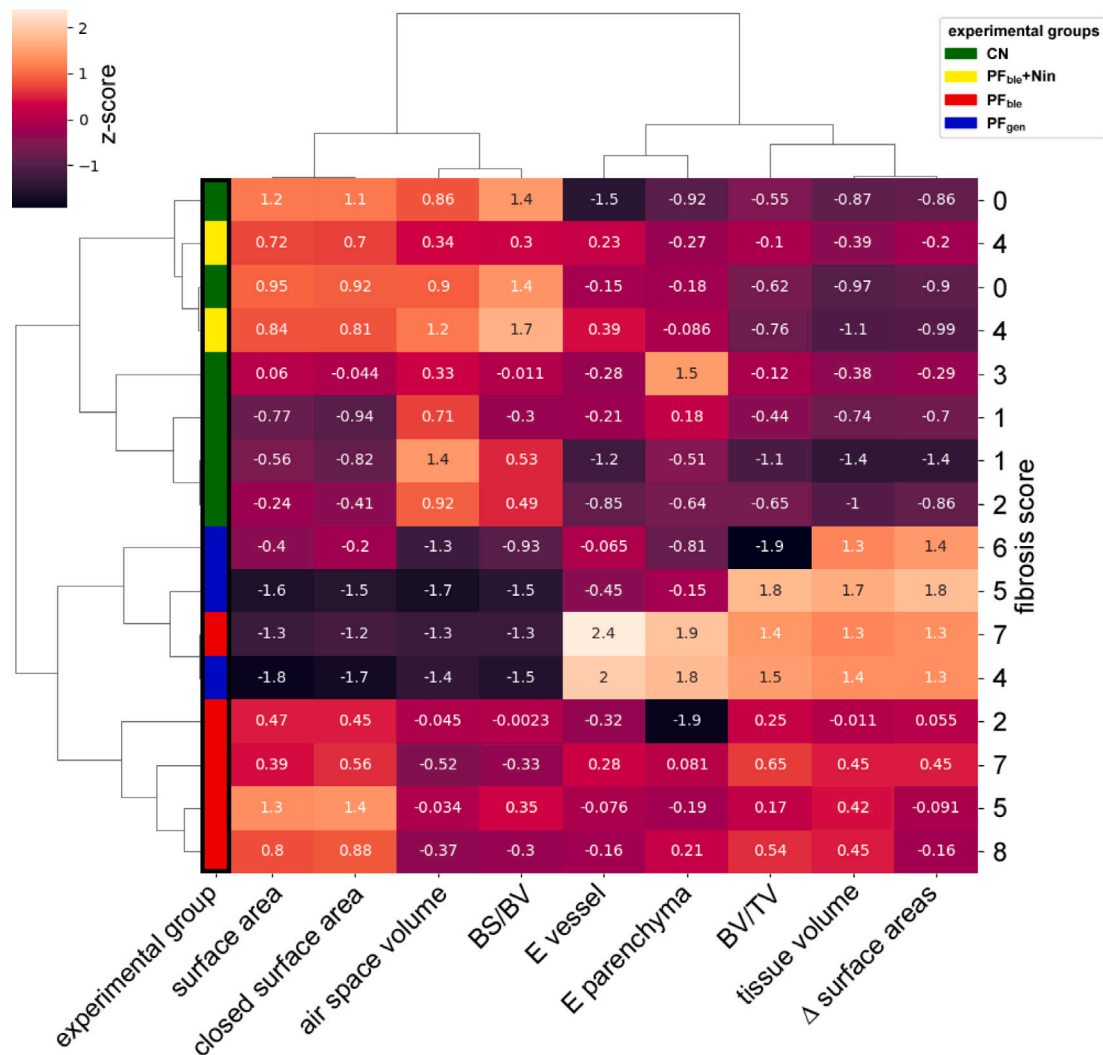
Fig. 8. Agglomerative clustering of the combined structural and AFM analysis. The Ashcroft score was used as label for comparison. On the highest hierarchy level, the data presents two clusters, successfully separating PF_{ble} mice (red) and PF_{gen} mice (blue) from CN mice (green) and the two additional mice treated with Nintedanib ($PF_{gen} + Nin$, yellow). At the next hierarchy level, PF_{ble} lungs can nearly perfectly be separated from lungs obtained from PF_{gen} mice, suggesting differences in the formed PF.

and does not interfere with the established diagnostic workflow allowing additional deep 3D and mechanic characterization of patient material. Additionally, this method is a suitable readout parameter for therapeutic response to drugs or genetic interventions as shown in Fig. 8 with the Nintedanib treated mice.

CRediT authorship contribution statement

Lorenzo D'Amico: Conceptualization, Data curation, Formal analysis, Investigation, Methodology, Software, Visualization, Writing – original draft, Writing – review & editing. **Angelika Svetlove:** Conceptualization, Data curation, Formal analysis, Software, Visualization, Writing – original draft, Writing – review & editing. **Elena Longo:** Data curation, Investigation, Writing – review & editing. **Ruth Meyer:** Formal analysis, Investigation, Writing – review & editing. **Beatrice Senigagliesi:** Formal analysis, Investigation, Validation, Writing – review & editing. **Giulia Saccomano:** Data curation, Formal analysis, Validation, Writing – review & editing. **Philipp Nolte:** Conceptualization, Methodology, Writing – review & editing. **Willi L. Wagner:** Conceptualization, Investigation, Methodology, Resources, Validation, Writing – review & editing. **Mark O. Wielpütz:** Supervision, Validation, Writing – review & editing. **Dominik H.W. Leitz:** Conceptualization, Investigation, Methodology, Resources, Validation, Writing – original draft, Writing –

review & editing. **Julia Duerr:** Data curation, Investigation, Validation, Writing – review & editing. **Marcus A. Mall:** Conceptualization, Resources, Supervision, Validation, Writing – review & editing. **Loredana Casalis:** Validation, Writing – review & editing. **Sarah Köster:** Conceptualization, Methodology, Resources, Validation, Writing – review & editing. **Frauke Alves:** Resources, Supervision, Validation, Writing – original draft, Writing – review & editing. **Giuliana Tromba:** Conceptualization, Funding acquisition, Investigation, Methodology, Project administration, Resources, Supervision, Validation, Writing – original draft, Writing – review & editing. **Christian Dullin:** Conceptualization, Data curation, Formal analysis, Investigation, Methodology, Software, Supervision, Validation, Visualization, Writing – original draft, Writing – review & editing.

Declaration of competing interest

Conflict of interest statement for the manuscript: None Declared

Acknowledgment

Funding

References

[1] F. Li, J. Deng, Y. Song, C. Wu, B. Yu, G. Wang, J. Li, Y. Zhong, F. Liang, Pulmonary fibrosis in patients with COVID-19: A retrospective study, Front. Cell. Infect. Microbiol. 12 (2022).

[2] P. Rivera-Ortega, C. Hayton, J. Blaikley, C. Leonard, N. Chaudhuri, Nintedanib in the management of idiopathic pulmonary fibrosis: clinical trial evidence and real-world experience, Ther. Adv. Respir. Dis. 12 (2018) 1753466618800618.

[3] R. Lattouf, R. Younes, D. Lutomski, N. Naaman, G. Godeau, K. Senni, S. Changotade, Picrosirius red staining: A useful tool to appraise collagen networks in normal and pathological tissues, J. Histochem. Cytochem. 62 (10) (2014) 751–758.

[4] R. Carrington, S. Jordan, S. Pitchford, C. Page, Use of animal models in IPF research, Pulm. Pharmacol. Ther. 51 (2018) 73–78.

[5] V. Della Latta, A. Cecchettini, S. Del Ry, M. Morales, Bleomycin in the setting of lung fibrosis induction: from biological mechanisms to counteractions, Pharmacol. Res. 97 (2015) 122–130.

[6] A. Moeller, K. Ask, D. Warburton, J. Gauldie, M. Kolb, The bleomycin animal model: a useful tool to investigate treatment options for idiopathic pulmonary fibrosis? Int. J. Biochem. Cell Biol. 40 (3) (2008) 362–382.

[7] J. Duerr, D.H.W. Leitz, M. Szczygiel, D. Dvornikov, S.G. Fraumann, C. Kreutz, P.K. Zadora, A. Seyhan Agircan, P. Konietzke, T.A. Engelmann, J. Hegermann, S. Mulugeta, H. Kawabe, L. Knudsen, M. Ochs, D. Rotin, T. Muley, M. Kreuter, F.J.F. Herth, M.O. Wielpütz, M.F. Beers, U. Klingmüller, M.A. Mall, Conditional deletion of Nedd4-2 in lung epithelial cells causes progressive pulmonary fibrosis in adult mice, Nature Commun. 11 (1) (2020) 2012, Number: 1 Publisher: Nature Publishing Group.

[8] D.H. Leitz, J. Duerr, S. Mulugeta, A. Seyhan Agircan, S. Zimmermann, H. Kawabe, A.H. Dalpke, M.F. Beers, M.A. Mall, Congenital deletion of Nedd4-2 in lung epithelial cells causes progressive alveolitis and pulmonary fibrosis in neonatal mice, Int. J. Mol. Sci. 22 (11) (2021) 6146.

[9] T.A. Engelmann, L. Knudsen, D.H. Leitz, J. Duerr, M.F. Beers, M.A. Mall, M. Ochs, Linking fibrotic remodeling and ultrastructural alterations of alveolar epithelial cells after deletion of Nedd4-2, Int. J. Mol. Sci. 22 (14) (2021) 7607.

[10] C.M. Evans, T.E. Fingerlin, M.I. Schwarz, D. Lynch, J. Kurche, L. Warg, I.V. Yang, D.A. Schwartz, Idiopathic pulmonary fibrosis: a genetic disease that involves mucociliary dysfunction of the peripheral airways, Physiol. Rev. 96 (4) (2016) 1567–1591.

[11] S.C. Mayo, A.W. Stevenson, S.W. Wilkins, In-line phase-contrast X-ray imaging and tomography for materials science, Materials 5 (12) (2012) 937–965.

[12] B. Bentivoglio-Ravasio, E. Marconi, L. Trotta, D. Dreossi, N. Sodini, L. Mancini, F. Zanini, C. Tonini, Synchrotron radiation microtomography of musical instruments: a non-destructive monitoring technique for insect infestations, J. Entomol. Acarol. Res. 43 (2) (2011) 149–155, Number: 2.

[13] A. Losso, A. Bär, B. Dämon, C. Dullin, A. Ganthaler, F. Petruzzellis, T. Savi, G. Tromba, A. Nardini, S. Mayr, B. Beikircher, Insights from in vivo micro-CT analysis: testing the hydraulic vulnerability segmentation in Acer pseudoplatanus and Fagus sylvatica seedlings, New Phytol. 221 (4) (2019) 1831–1842, _eprint: https://onlinelibrary.wiley.com/doi/pdf/10.1111/nph.15549.

[14] R. Lewis, Medical applications of synchrotron radiation x-rays, Phys. Med. Biol. 42 (7) (1997) 1213.

[15] M. Saccomano, J. Albers, G. Tromba, M. Dobrivojević Radmilović, S. Gajović, F. Alves, C. Dullin, Synchrotron inline phase contrast μCT enables detailed virtual histology of embedded soft-tissue samples with and without staining, J. Synchrotron Radiat. 25 (4) (2018) 1153–1161, _eprint: https://onlinelibrary.wiley.com/doi/pdf/10.1107/S1600577518005489.

[16] J. Albers, S. Pacilé, M.A. Markus, M. Wiart, G. Vande Velde, G. Tromba, C. Dullin, X-ray-based 3D virtual histology—Adding the next dimension to histological analysis, Mol. Imaging Biol. 20 (5) (2018) 732–741.

[17] J. Albers, A. Svetlove, J. Alves, A. Kraupner, F. di Lillo, M.A. Markus, G. Tromba, F. Alves, C. Dullin, Elastic transformation of histological slices allows precise co-registration with microCT data sets for a refined virtual histology approach, Sci. Rep. 11 (1) (2021) 10846, Number: 1 Publisher: Nature Publishing Group.

[18] O.L. Katsamenis, M. Olding, J.A. Warner, D.S. Chatelet, M.G. Jones, G. Sgalla, B. Smit, O.J. Larkin, I. Haig, L. Richeldi, I. Sinclair, P.M. Lackie, P. Schneider, X-ray micro-computed tomography for nondestructive three-dimensional (3D) X-ray histology, Amer. J. Pathol. 189 (8) (2019) 1608–1620.

[19] J.P. Desai, F. Moustarah, Pulmonary compliance, in: StatPearls, StatPearls Publishing, Treasure Island (FL), 2023.

[20] H.-J. Butt, B. Cappella, M. Kappl, Force measurements with the atomic force microscope: Technique, interpretation and applications, Surf. Sci. Rep. 59 (1–6) (2005) 1–152.

[21] F. Bano, L. Fruk, B. Sanavio, M. Glettenberg, L. Casalis, C.M. Niemeyer, G. Scoles, Toward multiprotein nanoarrays using nanografting and DNA directed immobilization of proteins, Nano Lett. 9 (7) (2009) 2614–2618, Publisher: American Chemical Society.

[22] D. Fotiadis, Imaging and manipulation of biological structures with the AFM, Micron 33 (4) (2002) 385–397.

[23] A. Calò, Y. Romin, R. Srouji, C.P. Zambirinis, N. Fan, A. Santella, E. Feng, S. Fujisawa, M. Turkekul, S. Huang, A.L. Simpson, M. D'Angelica, W.R. Jarnagin, K. Manova-Todorova, Spatial mapping of the collagen distribution in human and mouse tissues by force volume atomic force microscopy, Sci. Rep. 10 (1) (2020) 15664.

[24] D.M. Walters, S.R. Kleeberger, Mouse models of bleomycin-induced pulmonary fibrosis, Curr. Prot. Pharmacol. 40 (1) (2008) 5.46.1–5.46.17, _eprint: https://onlinelibrary.wiley.com/doi/pdf/10.1002/0471141755.ph0546s40.

[25] A. Khan, A. Markus, T. Rittmann, J. Albers, F. Alves, S. Hülsmann, C. Dullin, Simple low dose radiography allows precise lung volume assessment in mice, Sci. Rep. 11 (1) (2021) 4163.

[26] C. Dullin, F. di Lillo, A. Svetlove, J. Albers, W. Wagner, A. Markus, N. Sodini, D. Dreossi, F. Alves, G. Tromba, Multiscale biomedical imaging at the SYRMEP beamline of Elettra - Closing the gap between preclinical research and patient applications, Phys. Open 6 (2021) 100050.

[27] D. Paganin, S.C. Mayo, T.E. Gureyev, P.R. Miller, S.W. Wilkins, Simultaneous phase and amplitude extraction from a single defocused image of a homogeneous object, J. Microsc. 206 (1) (2002) 33–40, _eprint: https://onlinelibrary.wiley.com/doi/pdf/10.1046/j.1365-2818.2002.01010.x.

[28] F. Brun, S. Pacilè, A. Accardo, G. Kourousias, D. Dreossi, L. Mancini, G. Tromba, R. Pugliese, Enhanced and flexible software tools for X-ray computed tomography at the Italian synchrotron radiation facility elettra, Fund. Inform. 141 (2–3) (2015) 233–243, Publisher: IOS Press.

[29] T. Ashcroft, J.M. Simpson, V. Timbrell, Simple method of estimating severity of pulmonary fibrosis on a numerical scale, J. Clin. Pathol. 41 (4) (1988) 467–470.

[30] F.M. Lartey, M. Rafat, M. Negahdar, A.V. Malkovskiy, X. Dong, S. Sun, M. Li, T. Doyle, J. Rajadas, E.E. Graves, B.W. Loo, P.G. Maxim, Dynamic CT imaging of volumetric changes in pulmonary nodules correlates with physical measurements of stiffness, Radiother. Oncol. 122 (2) (2017) 313–318.

[31] A.I. Gómez-Varela, D.R. Stamov, A. Miranda, R. Alves, C. Barata-Antunes, D. Dambournet, D.G. Drubin, S. Paiva, P.A.A. De Beule, Simultaneous co-localized super-resolution fluorescence microscopy and atomic force microscopy: combined SIM and AFM platform for the life sciences, Sci. Rep. 10 (1) (2020) 1122, Number: 1 Publisher: Nature Publishing Group.

[32] A. Anura, D. Das, M. Pal, R.R. Paul, S. Das, J. Chatterjee, Nanomechanical signatures of oral submucous fibrosis in sub-epithelial connective tissue, J. Mech. Behav. Biomed. Mater. 65 (2017) 705–715.